Observation of Berry's Phase in a Solid-State Qubit

P. J. Leek,[1]* J. M. Fink,[1] A. Blais,[2] R. Bianchetti,[1] M. Göppl,[1] J. M. Gambetta,[3,4] D. I. Schuster,[4] L. Frunzio,[4] R. J. Schoelkopf,[4] A. Wallraff[1]*

In quantum information science, the phase of a wave function plays an important role in encoding information. Although most experiments in this field rely on dynamic effects to manipulate this information, an alternative approach is to use geometric phase, which has been argued to have potential fault tolerance. We demonstrated the controlled accumulation of a geometric phase, Berry's phase, in a superconducting qubit; we manipulated the qubit geometrically by means of microwave radiation and observed the accumulated phase in an interference experiment. We found excellent agreement with Berry's predictions and also observed a geometry-dependent contribution to dephasing.

When a quantum mechanical system evolves cyclically in time such that it returns to its initial physical state, its wave function can acquire a geometric phase factor in addition to the familiar dynamic phase (*1*, *2*). If the cyclic change of the system is adiabatic, this additional factor is known as Berry's phase (*3*), which, in contrast to the dynamic phase, is independent of energy and time.

In quantum information science (*4*), a prime goal is to use coherent control of quantum systems to process information, accessing a regime of computation unavailable in classical systems. Quantum logic gates based on geometric phases have been demonstrated in both nuclear magnetic resonance (*5*) and ion trap–based quantum information architectures (*6*). Superconducting circuits (*7*, *8*) are a promising solid-state platform for quantum information processing (*9*–*14*), in particular because of their potential scalability. Proposals for the observation of geometric phase in superconducting circuits (*15*–*19*) have existed since shortly after the first coherent quantum effects were demonstrated in these systems (*20*).

Geometric phases are closely linked to the classical concept of parallel transport of a vector on a curved surface. Consider, for example, a tangent vector $\mathbf{v}$ on the surface of a sphere being transported from the sphere's north pole around the path P shown in Fig. 1A, with $\mathbf{v}$ pointing south at all times. The final state of the vector $\mathbf{v}_f$ is rotated with respect to its initial state $\mathbf{v}_i$ by an angle ϕ equal to the solid angle subtended by the path P at the origin. Thus, this angle is dependent on the geometry of the path P and is independent of the rate at which it is traversed. As a result, departures from the original path that leave the solid angle unchanged will not modify ϕ. This robustness has been interpreted as a potential fault tolerance when applied to quantum information processing (*5*).

The analogy of the quantum geometric phase with the above classical picture is particularly clear in the case of a two-level system (a qubit) in the presence of a bias field that changes in time. A familiar example is a spin-½ particle in a changing magnetic field. The general Hamiltonian for such a system is $H = \hbar\mathbf{R} \cdot \boldsymbol{\sigma}/2$, where $\boldsymbol{\sigma} = (\sigma_x, \sigma_y, \sigma_z)$ are the Pauli operators, $\hbar$ is Planck's constant divided by 2π, and $\mathbf{R}$ is the bias field vector, expressed in units of angular frequency. The qubit dynamics is best visualized in the Bloch sphere picture, in which the qubit state $\mathbf{s}$ continually precesses about the vector $\mathbf{R}$, acquiring dynamic phase $\delta(t)$ at a rate $R = |\mathbf{R}|$ (Fig. 1B). When the direction of $\mathbf{R}$ is now changed adiabatically in time (i.e., at a rate slower than R), the qubit additionally acquires Berry's phase while remaining in the same superposition of eigenstates with respect to the quantization axis $\mathbf{R}$. The path followed by $\mathbf{R}$ in the three-dimensional parameter space of the Hamiltonian (Fig. 1C) is the analog of a path in real space in the classical case. When $\mathbf{R}$ completes the closed circular path C, the geometric phase acquired by an eigenstate is $\pm\Theta_C/2$ (*3*), where Θ_C is the solid angle of the cone subtended by C at the origin. The $\pm$ sign refers to the opposite phases acquired by the ground or excited state of the qubit, respectively. For the circular path shown in Fig. 1C, the solid angle is given by $\Theta_C = 2\pi(1 - \cos\theta)$, depending only on the cone angle θ.

We describe an experiment carried out on an individual two-level system realized in a superconducting electronic circuit. The qubit is a Cooper-pair box (*21*, *22*) with an energy level separation of $\hbar\omega_a \approx h \times 3.7$ GHz when biased at charge degeneracy, where it is optimally protected from charge noise (*23*). The qubit is embedded in a one-dimensional microwave transmission line res-

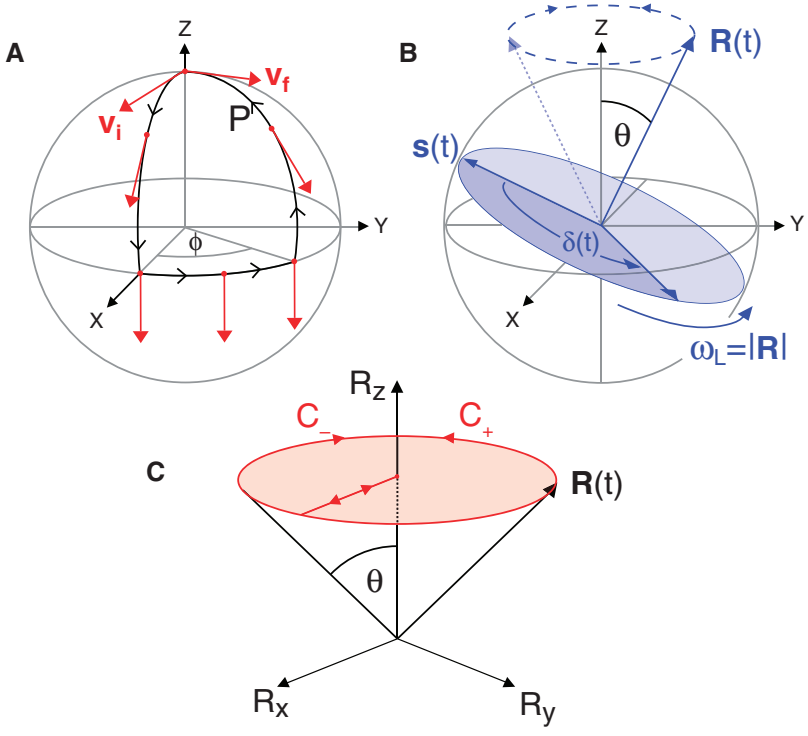

Fig. 1. (**A**) Parallel transport of the vector $\mathbf{v}_i$ on a spherical surface around the closed path P results in it rotating by a geometric angle ϕ to $\mathbf{v}_f$ when it returns to its initial position. (**B**) Dynamics of the Bloch vector $\mathbf{s}$ of a qubit in the presence of a bias field $\mathbf{R}$ tilted by an angle θ from the z axis. The vector $\mathbf{s}$ precesses about $\mathbf{R}$ at the Larmor rate $\omega_L = |\mathbf{R}|$. (**C**) Parameter space of the Hamiltonian for the same case.

[1]Department of Physics, Eidgenössische Technische Hochschule (ETH) Zürich, Schafmattstrasse 16, 8093 Zürich, Switzerland. [2]Département de Physique, Université de Sherbrooke, Sherbrooke, Québec J1K 2R1, Canada. [3]Institute for Quantum Computing and Department of Physics and Astronomy, University of Waterloo, Waterloo, Ontario N2L 3G1, Canada. [4]Departments of Applied Physics and Physics, Yale University, New Haven, CT 06520, USA.

*To whom correspondence should be addressed. E-mail: leek@phys.ethz.ch (P.J.L.); andreas.wallraff@phys.ethz.ch (A.W.)

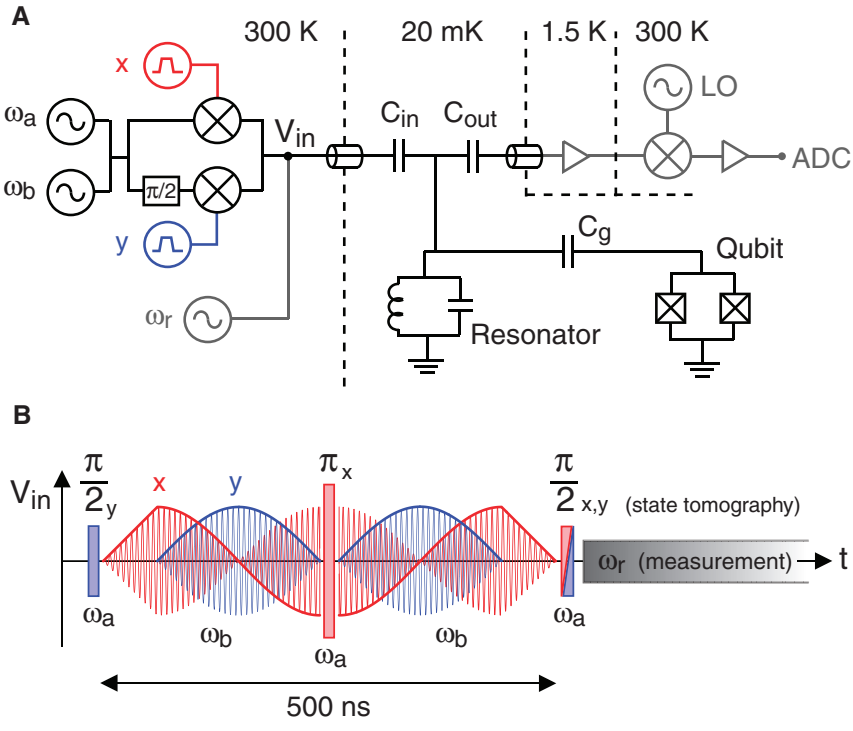

Fig. 2. (**A**) Simplified circuit diagram of the experimental setup. In the center at 20 mK is the resonator-qubit system, with the resonator represented by a parallel inductance and capacitance, and the qubit, a split Cooper-pair box, capacitively coupled to the resonator through C_g. The resonator is coupled to input and output transmission lines via the capacitors C_{in} and C_{out}. Three different pulse-modulated microwave frequency signals are applied to the resonator input. The two signals required for qubit manipulation, one at the qubit transition frequency $\omega_a/2\pi$ and a detuned signal $\omega_b/2\pi$, are modulated using mixers to the pattern shown in (B). The signal at the resonator frequency $\omega_r/2\pi$, used to measure the qubit state, is turned on after the pulse sequence is applied. (**B**) Schematic pulse sequence for the case $n = 0.5$. Resonant pulses, shown as shaded rectangles, are 12 ns in length. The two quadrature bias microwave fields (x, red; y, blue) are represented as sinusoids with modulation amplitude shown by solid lines. The linear ramps at the start and end of these sections correspond to moving adiabatically from $\Omega_R = 0$ to the circle of constant Ω_R depicted in Fig. 1C.

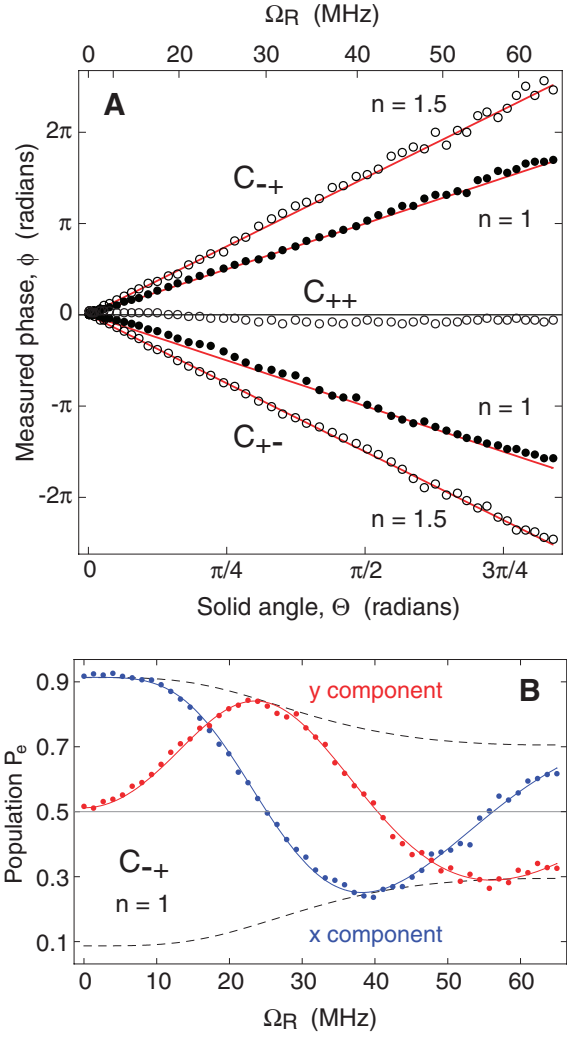

Fig. 3. (**A**) Measured phase ϕ versus solid angle Θ of a single conical path (lower axis). The applied microwave field amplitude is indicated on the upper axis (in units of the induced Rabi frequency Ω_R for resonant driving). Solid circles correspond to experiments in which $n = 1$ circular paths are traversed during each half of the spin-echo sequence, and open circles to the case $n = 1.5$. Subscripts ± of labels $C_{\pm\pm}$ correspond to the path direction before and after the spin-echo π pulse. Red solid lines are of slope $n = \pm1, \pm1.5$. The C_{++} experiment was carried out with $n = 1.5$. (**B**) State tomography data for the C_{-+} experiment with $n = 1$. Plotted is the qubit excited-state population after tomography pulses to extract $\langle\sigma_x\rangle$ [blue, $p_e = (\langle\sigma_x\rangle + 1)/2$] and $\langle\sigma_y\rangle$ [red, $p_e = (\langle\sigma_y\rangle + 1)/2$]. Lines are fits to Berry's phase, with a geometric dephasing envelope function (dashed lines, described in the text and Fig. 4). In all cases, the total pulse sequence time is $T = 500$ ns and the detuning is $\Delta/2\pi \approx 50$ MHz. Sequences are repeated 2×10^5 times to accumulate measurement statistics.

onator with resonance frequency $\omega_r/2\pi \approx 5.4$ GHz (Fig. 2A). In this architecture, known as circuit quantum electrodynamics (QED) (*24*, *25*), the qubit is isolated effectively from its electromagnetic environment, leading to a long energy relaxation time of $T_1 \approx 10$ μs and a spin-echo phase coherence time of $T_2^{echo} \approx 2$ μs. In addition, the architecture allows for a high-visibility dispersive readout of the qubit state (*26*).

Fast and accurate control of the bias field **R** for this superconducting qubit is achieved through phase and amplitude modulation of microwave radiation coupled to the qubit through the input port of the resonator (Fig. 2A). The qubit Hamiltonian in the presence of such radiation is

$$H = \frac{\hbar}{2}\omega_a\sigma_z + \hbar\Omega_R\cos(\omega_b t + \varphi_R)\sigma_x \quad (1)$$

where $\hbar\Omega_R$ is the dipole interaction strength between the qubit and a microwave field of frequency ω_b and phase φ_R, and t is time. Thus, $\Omega_R/2\pi$ is the Rabi frequency that results from resonant driving. The above Hamiltonian may be transformed to a frame rotating at the frequency ω_b by means of the unitary transformation

$$H' = UHU^{-1} - i\hbar\dot{U}U^{-1} \quad (2)$$

where $U = \exp(i\omega_b t\sigma_z/2)$, and $\dot{U}$ denotes its time derivative. Ignoring terms oscillating at $2\omega_b$ (the rotating wave approximation), the transformed Hamiltonian takes the form

$$H' \approx \frac{\hbar}{2}(\Delta\sigma_z + \Omega_x\sigma_x + \Omega_y\sigma_y) \quad (3)$$

where $\Omega_x = \Omega_R\cos\varphi_R$ and $\Omega_y = \Omega_R\sin\varphi_R$. This is equivalent to the generic situation depicted in

Fig. 1, B and C, where $\mathbf{R} = (\Omega_x, \Omega_y, \Delta)$ and $\Delta = \omega_a - \omega_b$ is the detuning between the qubit transition frequency and the applied microwave frequency. In our experiment, we keep Δ fixed and control the bias field to trace circular paths of different radii Ω_R.

We measure Berry's phase in a Ramsey fringe interference experiment by initially preparing an equal superposition of the qubit ground and excited states, which acquires a relative geometric phase $\gamma_C = 2\pi(1 - \cos\theta)$, equal to the total solid angle enclosed by the cone depicted in Fig. 1C, with $\cos\theta = \Delta/(\Omega_R^2 + \Delta^2)^{1/2}$. As the bias field adiabatically follows the closed path $C_\pm$, the qubit state acquires both a dynamic phase $\delta(t)$ and a geometric phase γ_C, corresponding to a total accumulated phase $\phi = \delta(t) \pm \gamma_C$ (the $\pm$ sign denoting path direction), which we extract by performing full quantum-state tomography (*4*). To directly observe only the geometric contribution, we use a spin-echo (*27*) pulse sequence that cancels the dynamic phase, as explained below.

The complete sequence (Fig. 2B) starts by preparing the initial σ_z superposition state with a resonant $\pi/2$ pulse. Then the path C_- is traversed, causing the qubit to acquire a phase $\phi_- = \delta(t) - \gamma_C$. Applying a resonant spin-echo π pulse to the qubit about an orthogonal axis now inverts the qubit state, effectively inverting the phase ϕ_- ; traversing the control field path again, but in the opposite direction C_+, adds an additional phase $\phi_+ = \delta(t) + \gamma_C$. This results in total in a purely geometric phase $\phi = \phi_+ - \phi_- = 2\gamma_C$ being acquired during the complete sequence, which we denote as C_{-+}. Note that unlike the geometric phase, the dynamic phase is insensitive to the path direction and hence is completely canceled.

At the end of the sequence, we extract the phase of the qubit state by means of quantum-state tomography. In our measurement technique (*26*), the z component of the qubit Bloch vector $\langle\sigma_z\rangle$ is determined by measuring the excited-state population $p_e = (\langle\sigma_z\rangle + 1)/2$. To extract the x and y components, we apply a resonant $\pi/2$ pulse rotating the qubit about either the x or y axis and then perform the measurement, revealing $\langle\sigma_y\rangle$ and $\langle\sigma_x\rangle$, respectively. The phase of the quantum state after application of the control sequence is then extracted as $\phi = \tan^{-1}(\langle\sigma_y\rangle/\langle\sigma_x\rangle)$.

In Fig. 3A we show the measured phase ϕ and its dependence on the solid angle of the path for a number of different experiments, all carried out at $\Delta/2\pi \approx 50$ MHz, and total pulse sequence time $T = 500$ ns. Three parameters are varied: the path radius Ω_R (upper x axis), the number n of circular loops traversed in each half of the spin-echo sequence, and the direction of traversal of the paths (C_{-+} and C_{+-}). The measured phase is in all cases seen to be linear in solid angle as Ω_R is swept, with a root-mean-square deviation across all data sets of 0.14 rad from the expected lines of slope $2n$. Thus, all results are in close agreement with the predicted Berry's phase, and it is clear that we are able to accurately control the amount of phase accumulated geometrically. Note also that the dynamic phase is indeed effectively eliminated by the spin echo. Reversing the overall direction of the paths is observed to invert the sign of the phase (Fig. 3A). Traversing the circular paths on either side of the spin-echo pulse in the same direction (C_{++}) as a control experiment results in zero measured phase (Fig. 3A).

Observation of a pure Berry's phase requires adiabatic qubit dynamics, which in turn requires the rate of rotation of the bias field direction to be much less than the Larmor rate R of the qubit in the rotating frame. For the case of constant cone angle θ, this translates to the requirement that the adiabaticity parameter $A = \dot{\varphi}_R \sin\theta/2R \ll 1$. If the Hamiltonian is changed nonadiabatically, the qubit state can no longer exactly follow the effective field $\mathbf{R}$, and the geometric phase acquired deviates from Berry's phase (*28*). For the experiments here, $A \leq 0.04$, and deviation of the measured phase from Berry's phase is not discernible. We have also verified experimentally that in this adiabatic limit, the observed phase is independent of the total sequence time T.

Figure 3B shows a measurement of the x and y components of the qubit state from which the Berry's phase is extracted. Interestingly, the visibility of the observed interference pattern is seen to have a dependence on Ω_R. Because the data were taken at a fixed total sequence time, this is not due to conventional T_2 dephasing, which is also independently observable as a function of time, but can be explained as due to geometric dephasing, an effect dependent on the geometry of the path (*29*).

In our experiment, dephasing is dominated by low-frequency fluctuations in the qubit transition frequency ω_a (and thus Δ) induced by charge noise coupling to the qubit (*30*). The spin-echo pulse sequence effectively cancels the dynamic dephasing due to the low-frequency noise. However, the geometric phase is sensitive to slow fluctuations, which cause the solid angle subtended by the path at the origin to change from one measurement to the next (Fig. 4A). The effect on the geometric phase of such fluctuations in the classical control parameters of the system has been studied theoretically (*29*). In the limit of the fluctuations being slower than the time scale of the spin-echo sequence, the variance of the geometric phase σ_γ^2 has itself a purely geometric dependence, $\sigma_\gamma^2 = \sigma_\omega^2(2n\pi\sin^2\theta/R)^2$, where σ_ω^2 is the variance of the fluctuations in ω_a (*29*). In Fig. 4B, we show the observed dependence of the coherence on geometry explicitly by plotting $(\langle\sigma_x\rangle^2 + \langle\sigma_y\rangle^2)^{1/2}$ versus Ω_R, which fits well to the expected dependence $\exp(-\sigma_\gamma^2/2)$. This is also in agreement with the raw data in Fig. 3B.

We have observed an important geometric contribution to dephasing that occurs when geometric operations are carried out in the presence of low-frequency fluctuations. In contrast, higher-frequency noise in ω_a is expected to have little influence on Berry's phase (provided adiabaticity is maintained), because its effect on the solid angle is averaged out (Fig. 4C). This characteristic robustness of geometric phases to high-frequency noise may be exploitable in the realization of logic gates for quantum computation, although the effect of geometric dephasing due to low-frequency noise must be taken into account.

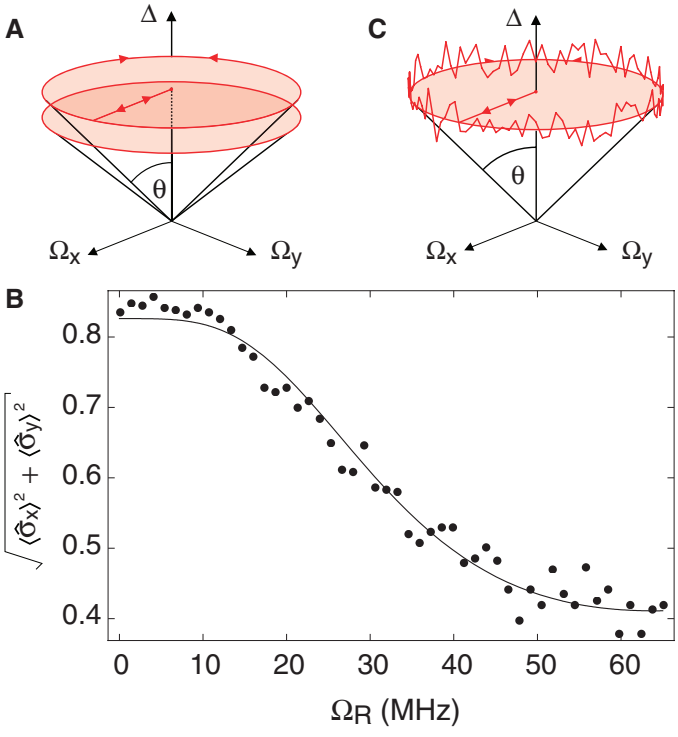

Fig. 4. (**A**) Low-frequency fluctuations in Δ change the solid angle enclosed by the path from one measurement to the next, and cause geometric dephasing with a characteristic dependence on the cone angle and bias field amplitude. (**B**) Magnitude of the equatorial component of the Bloch vector $(\langle\sigma_x\rangle^2 + \langle\sigma_y\rangle^2)^{1/2}$ for the data shown in Fig. 3B, plotted as a function of drive amplitude Ω_R. The fit is to a geometric dephasing factor $\exp(-\sigma_\gamma^2/2)$, where σ_γ^2 is the variance of the geometric phase. (**C**) The conical parameter space path in the presence of high-frequency ($f >> T^{-1}$) noise in Δ, having no effect on the total solid angle.

References and Notes

1. A. Shapere, F. Wilczek, *Geometric Phases in Physics* (World Scientific, Singapore, 1989).

2. J. Anandan, *Nature* **360**, 307 (1992).
3. M. V. Berry, *Proc. R. Soc. London Ser. A* **392**, 45 (1984).
4. M. A. Nielsen, I. L. Chuang, *Quantum Computing and Quantum Information* (Cambridge Univ. Press, Cambridge, 2000).
5. J. A. Jones, V. Vedral, A. Ekert, G. Castagnoli, *Nature* **403**, 869 (2000).
6. D. Leibfried *et al.*, *Nature* **422**, 412 (2003).
7. G. Wendin, V. Shumeiko, *Handbook of Theoretical and Computational Nanotechnology*, M. Rieth, W. Schommers, Eds. (American Scientific, Los Angeles, 2006), vol. 3 (www.arxiv.org/abs/cond-mat/0508729v1).
8. M. H. Devoret, A. Wallraff, J. M. Martinis, www.arxiv.org/abs/cond-mat/0411174v1 (2004).
9. T. Yamamoto, Y. A. Pashkin, O. Astafiev, Y. Nakamura, J. S. Tsai, *Nature* **425**, 941 (2003).
10. M. Steffen *et al.*, *Science* **313**, 1423 (2006).
11. A. O. Niskanen *et al.*, *Science* **316**, 723 (2007).
12. J. H. Plantenberg, P. C. de Groot, C. J. P. M. Harmans, J. E. Mooij, *Nature* **447**, 836 (2007).
13. J. Majer *et al.*, *Nature* **449**, 443 (2007).
14. M. A. Sillanpää, J. I. Park, R. W. Simmonds, *Nature* **449**, 438 (2007).
15. G. Falci, R. Fazio, G. M. Palma, J. Siewert, V. Vedral, *Nature* **407**, 355 (2000).
16. X. B. Wang, M. Keiji, *Phys. Rev. B* **65**, 172508 (2002).
17. A. Blais, A. M. S. Tremblay, *Phys. Rev. A* **67**, 012308 (2003).
18. Z. H. Peng, M. J. Zhang, D. N. Zheng, *Phys. Rev. B* **73**, 020502 (2006).
19. M. Mottonen, J. P. Pekola, J. J. Vartiainen, V. Brosco, F. W. J. Hekking, *Phys. Rev. B* **73**, 214523 (2006).
20. Y. Nakamura, Y. A. Pashkin, J. S. Tsai, *Nature* **398**, 786 (1999).
21. A. Shnirman, G. Schön, Z. Hermon, *Phys. Rev. Lett.* **79**, 2371 (1997).
22. V. Bouchiat, D. Vion, P. Joyez, D. Esteve, M. H. Devoret, *Phys. Scr.* **T76**, 165 (1998).
23. D. Vion *et al.*, *Science* **296**, 886 (2002).
24. A. Blais, R. S. Huang, A. Wallraff, S. M. Girvin, R. J. Schoelkopf, *Phys. Rev. A* **69**, 062320 (2004).
25. A. Wallraff *et al.*, *Nature* **431**, 162 (2004).
26. A. Wallraff *et al.*, *Phys. Rev. Lett.* **95**, 060501 (2005).
27. A. Abragam, *Principles of Nuclear Magnetism* (Oxford Univ. Press, Oxford, 1961).
28. Y. Aharonov, J. Anandan, *Phys. Rev. Lett.* **58**, 1593 (1987).
29. G. De Chiara, G. M. Palma, *Phys. Rev. Lett.* **91**, 090404 (2003).
30. G. Ithier *et al.*, *Phys. Rev. B* **72**, 134519 (2005).

31. We thank P. Maurer and L. Steffen for their contributions to the project, and A. Shnirman, J. Blatter, G. De Chiara, and G. M. Palma for valuable discussions. Supported by the EC via an Intra-European Marie Curie Fellowship (P.J.L.), the Natural Sciences and Engineering Research Council of Canada, Canadian Institute for Advanced Research, and Fonds Québécois de la Recherche sur la Nature et les Technologies (A.B.), the National Security Agency under the Army Research Office, NSF, and Yale University (D.I.S., L.F., and R.J.S.), Consiglio Nazionale delle Ricerche–Istituto di Cibernetica, Pozzuoli, Italy (L.F.), the Ontario Research Development Challenge Fund and Mathematics of Information Technology and Complex Systems (J.M.G.), the Swiss National Science Foundation, and ETH Zürich.

29 August 2007; accepted 1 November 2007
Published online 22 November 2007;
10.1126/science.1149858
Include this information when citing this paper.

High-Performance Carbon Nanotube Fiber

Krzysztof Koziol,[1] Juan Vilatela,[1] Anna Moisala,[1] Marcelo Motta,[1] Philip Cunniff,[2] Michael Sennett,[2] Alan Windle[1]*

With their impressive individual properties, carbon nanotubes should form high-performance fibers. We explored the roles of nanotube length and structure, fiber density, and nanotube orientation in achieving optimum mechanical properties. We found that carbon nanotube fiber, spun directly and continuously from gas phase as an aerogel, combines high strength and high stiffness (axial elastic modulus), with an energy to breakage (toughness) considerably greater than that of any commercial high-strength fiber. Different levels of carbon nanotube orientation, fiber density, and mechanical properties can be achieved by drawing the aerogel at various winding rates. The mechanical data obtained demonstrate the considerable potential of carbon nanotube assemblies in the quest for maximal mechanical performance. The statistical aspects of the mechanical data reveal the deleterious effect of defects and indicate strategies for future work.

High-performance synthetic fibers, based on polymer molecules or graphene sheets, have been under development for the past half century, motivated by the high strength and stiffness of the covalent carbon-carbon bond and by the ability to achieve alignment of these bonds with the fiber axis. The key to producing such fibers is to maximize the number of covalently bonded carbon atoms per unit volume or mass, and thus to reduce the proportion of other types of atoms or groups attached to polymer chains. The advantage of pure carbon fibers is that the mechanical properties are derived from the in-plane stiffness and strength of graphene sheets, without the adulterating effect of additional atoms to satisfy available carbon bonds. However, the route to carbon fibers involves the alignment of precursor structures, which are then covalently bonded to each other to create the final structure. This second phase of chemistry not only complicates the processing operation, but also creates a structure in which the basic mechanism that generates toughness in linear polymer systems (i.e., chain pullout) is not available. Carbon fibers are thus comparatively brittle, especially when they are heat-treated to maximize stiffness.

The very high axial strength and stiffness of individual carbon nanotubes, demonstrated both by experiment (*1*–*3*) and modeling (*4*–*6*), opens up the possibility of processing them directly into fibers without the need for a subsequent cross-linking step. Thus, the benefits of high-performance polymeric fibers—especially directness of processing and fiber toughness (measured as energy absorbed up to fracture)—can be combined with the advantages of a fiber consisting only of carbon atoms. If one views carbon nanotubes as extremely strong and stiff polymer molecules, it is not surprising that the processing routes developed so far borrow concepts from polymer fiber–processing technologies. The leading approaches for production of nanotube fibers are (i) spinning from a lyotropic liquid crystalline suspension of nanotubes, in a process similar to that used for polymeric fibers such as aramids (*7*); (ii) spinning from multiwall nanotubes previously grown on a substrate as semi-aligned carpets (*8*, *9*); and (iii) spinning directly from an aerogel of single- and double-walled carbon nanotubes as they are formed in a chemical vapor deposition reactor (*10*). This last process is the one we used (*11*). In terms of mechanical properties, the various techniques have met with different degrees of success. Fibers produced by the liquid crystalline route (*7*) showed an encouraging stiffness of 120 GPa but only modest strengths on the order of 0.1 GPa. Fibers spun from carbon nanotube carpets and subsequently twisted (*9*) have now been made (*12*) with strengths up to 1.9 GPa and stiffnesses up to 330 GPa. An individual strength value of 3.3 GPa was also mentioned (*13*). Until now, the highest strength reported for direct-spun carbon nanotube fiber was 2.2 GPa, and the highest stiffness reported was 160 GPa (*14*).

The mechanical properties of a material are limited by defects within an otherwise perfect structure. In the case of high-performance polymer fibers, these defects consist of chain ends and

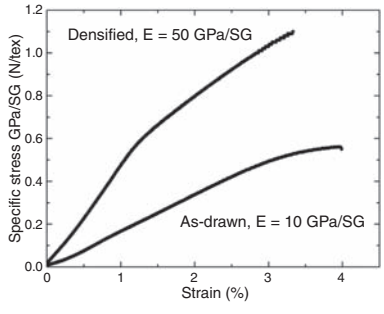

Fig. 1. Specific stress-strain curves for an as-drawn fiber and an acetone-densified fiber. These curves are as-recorded, and the gauge length in each case was 20 mm.

[1]Department of Materials Science, University of Cambridge, Pembroke Street, Cambridge CB2 3QZ, UK. [2]U.S. Army, Natick Soldier Research Development and Engineering Center, 15 Kansas Street, Natick, MA 01760, USA.

*To whom correspondence should be addressed. E-mail: ahw1@hermes.cam.ac.uk